

Target shape effects on monoenergetic GeV proton acceleration

Min Chen,¹ Tong-Pu Yu,^{1,2} Alexander Pukhov,^{1,*} and Zheng-Ming Sheng³

¹*Institut für Theoretische Physik I, Heinrich-Heine-Universität Düsseldorf, 40225 Düsseldorf, Germany*

²*Department of Physics, National University of Defense Technology, Changsha 410073, China*

³*Department of Physics, Shanghai Jiao Tong University, Shanghai 200240, China*

and Beijing National Laboratory of Condensed Matter Physics, Institute of Physics, Beijing 100080, China

When a circularly polarized laser pulse interacts with a foil target, there are three stages: pre-hole-boring, hole-boring and the light sail acceleration. We study the electron and ion dynamics in the first stage and find the minimum foil thickness requirement for a given laser intensity. Based on this analysis, we propose to use a shaped foil for ion acceleration, whose thickness varies transversely to match the laser intensity. Then, the target evolves into three regions: the acceleration, transparency and deformation regions. In the acceleration region, the target can be uniformly accelerated producing a mono-energetic and spatially collimated ion beam. Detailed numerical simulations are performed to check the feasibility and robustness of this scheme, such as the influence of shape factors and surface roughness. A GeV mono-energetic proton beam is observed in the three dimensional particle-in-cell simulations when a laser pulse with the focus intensity of 10^{22} W/cm^2 is used. The energy conversion efficiency of laser pulse to accelerated proton beam is more than 23%. Synchrotron radiation and damping effects are also checked in the interaction.

PACS numbers: 52.40.Nk, 52.35.Mw, 52.57.Jm, 52.65.Rr

I. INTRODUCTION

Ion acceleration is one of the most important topics in the ultrashort ultraintense (USUI) laser-plasma accelerator field [1, 2, 3, 4]. Because the laser-accelerated proton and ion beams are highly concentrated, ultrashort and ultraintense, they have a broad spectrum of potential applications, such as proton therapy [5], proton imaging [6], ion beam ignition of laser fusion targets [7], *etc.* These applications usually require a high degree of beam monochromaticity as well.

The usual energy spectrum of the ion beams produced due to the mechanism of target normal sheath acceleration (TNSA) shows an exponential decay up to a high energy cutoff. To overcome this, a few schemes are proposed such as use of plasma lens [8, 9], double layer targets [10] and special target shaping [11, 12, 13, 14].

It was shown recently in theoretical analysis and numerical simulations that when a circularly polarized (CP) pulse is used, high energy mono-energetic ion acceleration can be achieved. The reason is absence of the oscillatory term in the ponderomotive force of a CP pulse and thus suppression of the electron heating [15]. A CP laser pulse pushes gently the whole electron fluid and generates a moving local charge separation field that accelerates ions. It looks as if the whole target is accelerated by the laser radiation pressure. The mechanism then is similar to the radiation pressure dominated acceleration (RPDA) proposed by Esirkepov *et al.* before [3]. However, the threshold for the laser intensity is dramatically reduced when a CP pulse is used. In the one dimensional geometry and if the laser pulse is long enough, the target can be accelerated in multi stages and in every stage the accelerated ions gain the same energy. The narrow width of the final energy spectrum is a result [16]. Certainly, the mechanism is sensitive to a laser prepulse as it might cause pre-plasma at the target surface and destroy the accelerating structure. Thanks to the development of USUI laser pulse and plasma mirror technology, this can be controlled in today's experiments.

Recently, Klimo *et al.* [17], Robinson *et al.* [18] and Yan *et al.* [19] have studied an ultra thin target condition. They have shown that ions are accelerated continuously and rotate in the phase space. This can be considered as a special kind of multi stage acceleration [20]. The second stage begins before the end of the first one. The width of the spectrum is further reduced and mono-energetic ion beams are easily observed. Qiao *et al.* [21] recently studied this kind of acceleration and separated it into two different processes: hole boring and light sail. They noticed the importance of the transition between these two processes to reach the final mono-energetic spectrum. In the hole boring process, the laser pulse propagates thorough the bulk of the foil target and compresses it. Afterwards, when the compressed layer arrives at the rear side of the foil, the light sail process begins. At this stage, the whole target dynamics can be well described using a ballistic equation [22]. There is a minimum target thickness for the target to

*To whom any corresponding should be sent: pukhov@tp1.uni-duesseldorf.de

stay opaque so that the process can operate. To get the minimum target thickness for acceleration, all of the earlier works use the balance between the laser pressure and the charge separation field and assume immobile ions during the balance build-up. This is correct when the laser intensity is relatively small and the target density is low. However, it overestimates the minimum target thickness when the laser intensity and target density increase.

In this paper we study the process of the balance build-up and name this process as a pre-hole-boring process. We consider the finite ion mass to calculate the minimum foil thickness for ion acceleration, which is usually also the optimal thickness. Then, we suggest to use a shaped target to achieve a uniform acceleration. For shaped targets, we find that the acceleration structure can be kept for a longer time compared with usual flat targets. The final spectrum contains a mono-energetic peak. Later we study the robustness of our scheme by considering the influence of the shape parameters and surface roughness on the final spectrum. This affords a detailed description to our recently published paper [23]. We also make some consideration on the radiation damping effect during the ion acceleration. Finally, we give some discussions and a summary.

II. PRE-HOLE-BORING AND OPTIMAL TARGET THICKNESS

Here, we study the electron and ion dynamics during the laser impinging. When the laser pulse arrives at the front surface of the target, electrons are accelerated and piled up by the laser pressure. Later, ions start to move being accelerated by the charge separation field. We call this stage pre-hole-boring since during this time ions have not caught up with the compressed electron layer (CEL), and the hole boring process did not reach its stationary stage yet.

For convenience we use normalized variables here. The laser electric field is normalized as $a = eE/m\omega c$, spatial and temporal coordinates are normalized by the laser wavelength λ and period $2\pi/\omega$, respectively. The particle velocity, mass, plasma density are normalized by light speed in vacuum c , electron mass m , and critical density $n_c = m\omega^2/4\pi e^2$, respectively.

If we consider only the ponderomotive force of the laser pulse acting on the plasma electrons (the light pressure), the dynamics of the CEL is governed by the equations:

$$n_0 l_1 \frac{d\gamma\beta}{dt} + n_0 \gamma \beta \frac{dl_1}{dt} = \frac{a_0^2}{\pi} \frac{1-\beta}{1+\beta} - \pi n_0^2 l_1 (l_1 + l_s) \quad (1)$$

$$\frac{dl_1}{dt} = \beta, \quad (2)$$

where β is the normalized velocity of the CEL, γ is the relativistic factor, l_1 is the displacement of the CEL, n_0 is the initial plasma density, a_0 is the laser electric field and l_s is the skin length for the laser pulse. The second term on the left side of the first equation comes from the mass increase of the CEL. The first term on the right side is the contribution of the laser pressure and the second one is due to the charge separation field.

We treat ions as a hydrodynamical fluid and solve the following hydrodynamical equations:

$$\frac{\partial n}{\partial t} + \frac{\partial(n\beta_i)}{\partial t} = 0, \quad (3)$$

$$\frac{\partial \beta_i}{\partial t} + \beta_i \frac{\partial \beta_i}{\partial x} = \frac{2\pi}{m_i} E_x, \quad (4)$$

$$\frac{\partial E_x}{\partial x} = 4\pi e(n - n_e) \quad (5)$$

where n is the ion fluid density, β_i is its velocity, m_i is the ion mass and E_x is the charge separation field. The density distribution of the electrons (n_e) is calculated from the evolution of the CEL. We simply assume the electrons from the front target are piled up, compressed and uniformly distributed within a region with the size of the skin length $l_s = 1/\sqrt{n_0}$. We do this because the CEL is always in front of the accelerated ions at this early stage. This assumption will become invalid as soon as the ions catch up with the CEL. Our calculation ends before this time and makes sure the hydrodynamic velocity of the ions at the density peak point is larger than the CEL velocity. The moving distance of the CEL at this time is just the one we are looking for and it equals the minimum thickness of the target for the ion acceleration (l_{hydro}). As we will see usually this gives a smaller value than the usually used one ($l_{imm} = a/\pi n$) obtained in the immobile ion model.

We solve the system of equations (1)-(5) numerically. In our calculations, we vary the ion mass, target density and laser intensity to see their effects on the minimum target thickness. The foil is assumed to be thick enough

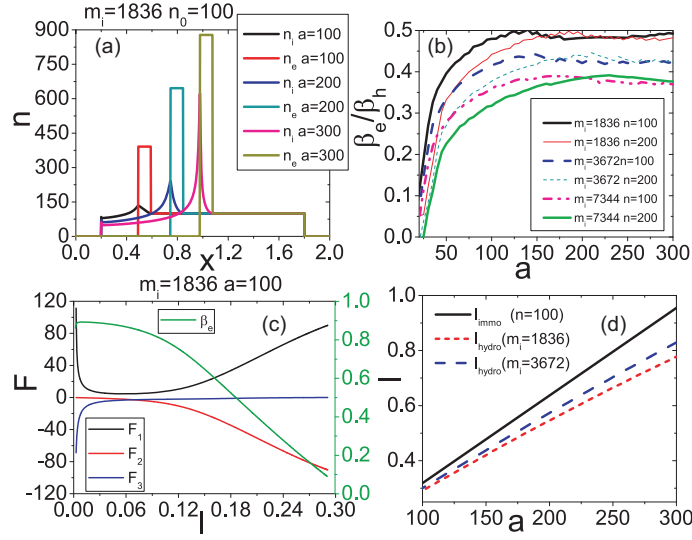


FIG. 1: Analytical results for the pre-hole-boring process. (a) Density distribution of the electrons and ions at the end of the numerical calculation. (b) The dependance of final velocity of the CEL at the end of the calculation on the laser intensity, target density and ion mass. (c) Evolution of CEL velocity and forces on the CEL along with the CEL displacement(l_1). (d) CEL displacements at the end of the calculation for different ion masses and laser intensities. The black solid line represents the minimum thickness obtained in an immobile ion model.

initially ($0.2\lambda < x < 1.8\lambda$) for the ions to catch up with the CEL. The electron and ion density distributions at the calculation end are shown in Fig. 1(a). The density distributions also indicate one of the necessary criterions to end our calculation: the time when the peak of the ion density distribution reaches the CEL. After this the charge separation field for CEL will deviate obviously from the one used in Eq. (1). The moving distance of the CEL at this time is assumed to be the minimum thickness of the target l_{hydro} since the ions can catch up with the CEL once the target is thicker than l_{hydro} . Obviously we can get l_{hydro} from the numerically calculations show in Fig. 1(a), it can also be gotten by considering the force balance as we will show in the following. Fig. 1(b) shows the ratio of the CEL velocity (β_e) at the end of the calculation to the theoretical relativistic hole boring velocity $\beta_h = a/(a + \sqrt{m_i n_0})$ [24]. As we see the value tends to a constant depending only on the ion mass. With this constant value it is then easy to calculate the displacement of the CEL at this time from the relationship of the almost balance between the charge separation force and the laser pressure:

$$\pi n_0^2 l_1 (l_1 + l_s) = \frac{a_0^2}{\pi} \frac{1 - \beta_e}{1 + \beta_e} \quad (6)$$

The force balance can be seen from Fig. 1(c). The black line indicates the force due to laser pressure, the red line indicates the charge separation force and the blue line indicates the force due to mass increase. The first two forces balance with each other very quickly once the CEL moves 0.1λ into the target. The displacements of the CEL obtained in Fig. 1(a) fit well with those gotten from the force balance calculation. The latter is in Fig. 1(d) with different ion masses. The usually used value based on the immobile ions model l_{immo} is also shown with the black line. As we see, when the intensity of the laser electric field is larger than $a_0 = 100$, the present results l_{hydro} are smaller than the value based on immobile ions l_{immo} . The lighter the ion mass, the larger the difference with the one of the immobile ion model. l_{hydro} is just the minimum thickness of the foil target for ion acceleration. When the target is thinner than this minimum value, ions can not catch up the electrons and neutralize them. Then electrons are smashed away from the ions completely by the light pressure and the target is transparent to the laser later. The electrons are dispersed by the pulse and the acceleration structure disappears. From the present calculation, we see that ions have already caught up with the electrons before the CEL moves a distance of l_{immo} and the CEL will not completely separate from the ions. So our model shows that the usual value l_{immo} overestimates the minimum thickness. This finding is especially important for the selection of the target thickness for multicascade ion acceleration scheme recently proposed by Gonoskov *et al.* [25].

FIG. 2: Layout of the interaction scheme. σ_T defines the transverse Gaussian profile of the shaped target, l_0 is the maximal target thickness while l_1 is the cutoff thickness. A circularly polarized laser pulse is incident on the foil target from the left boundary.

III. ION ACCELERATION BY USE OF SHAPED FOIL TARGET

Up to now we discussed the minimum target thickness for ion acceleration in the laser pressure dominated regime. Once the target is thicker than the minimum value, the whole target is opaque to the laser pulse and it is accelerated in a hole-boring process with the velocity β_h . When the CEL arrives at the rear of the foil, the acceleration changes to a light sail process. Then, the momentum evolution of the target satisfies [18, 26]:

$$\frac{dp}{dt} = \frac{2I}{c} \frac{\sqrt{p^2 + \sigma^2 c^2} - p}{\sqrt{p^2 + \sigma^2 c^2} + p}, \quad (7)$$

where I is the laser intensity, σ is the target area density. For the velocity evolution of the target one obtains:

$$\frac{d\beta}{dt} = \frac{1}{2\pi n_0 m_i c} \frac{E^2(t, x, r)}{l_0} \frac{1}{\gamma^3} \frac{1 - \beta}{1 + \beta}. \quad (8)$$

Here E is the laser electric field amplitude, n_0 and l_0 are the target initial density and thickness, respectively.

Eq. (8) shows that the energy spread of accelerated ions depends on the transverse variation of the local ratio of laser intensity to the target area density. The distance the ions pass under the laser pressure is $s(r) \propto E^2(t, x, r) l_0^{-1}$. An initially flat target is inevitably deformed, if the laser intensity is not uniform transversely. The target deformation quickly destroys the acceleration structure and deteriorates the beam quality. From Eq. (8) we see that a target can be uniformly accelerated if its areal density σ is shaped properly. For the usual transversely Gaussian pulse [$a = a_0 \exp(-r^2/\sigma_L^2)$], one can use a target with the Gaussian thickness distribution as shown in Fig. 2. In the following simulations, the distribution of the target thickness along the transverse direction is:

$$l = \max\{l_1, l_0 \times \exp[(-r^2/\sigma_T^2)^m]\}. \quad (9)$$

Here r is the transverse distance to the laser axis, l_1, l_0, σ_T, m are the shape factors, which are marked in Fig. 2.

Before carrying out the simulations for such kind of shaped target, we first check the target transparency for the pulse with a transversely Gaussian pulse. In Fig. 3 we show the minimum thickness requirement from theoretical calculation by use of Eq. (6) and the acceleration factor $F_{acc} = a^2/l$ in the target transverse direction. β_e is the function of a, n, m_i and we get the value from Fig. 1(b). The shaped target thickness and flat target thickness distributions are also shown in the figure. As we see from Fig. 3(a) for the shaped target, in the center it is thicker than the minimum value l_{min} . At this region, the acceleration factor F_{acc} is also almost uniform, so the target can be accelerated uniformly. Outside of this region, the target thickness is thinner than l_{min} . The target is transparent to the laser pulse here, ions can not get an effective uniform acceleration. In the outside region, the target is thicker than l_{min} again and F_{acc} decreases with radius, so in this region the target is opaque and will be accelerated and deformed. However, for the usual flat target [see Fig. 3(b)], the target thickness is always larger than the minimum

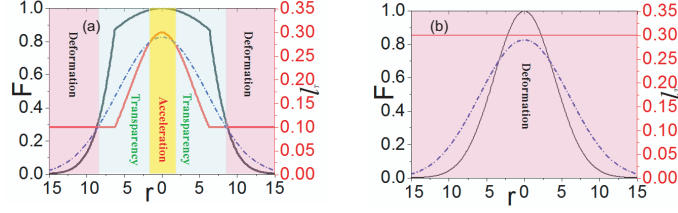


FIG. 3: Target partitions in the cases of (a) shaped target and (b) flat target, according to the transparency calculation. The parameters for the shaped target are: $l_0 = 0.3\lambda$, $l_1 = 0.1\lambda$, $m = 1$, $\sigma_T = 6\lambda$. For the flat target we just use $l_1 = l_0 = 0.3\lambda$. The laser pulse has a focus of $\sigma_L = 8\lambda$. The red solid line represents the target thickness distribution along the transverse direction; the blue dashed line represents the minimum target thickness requirement for an opaque target. The black line represents the acceleration factor.

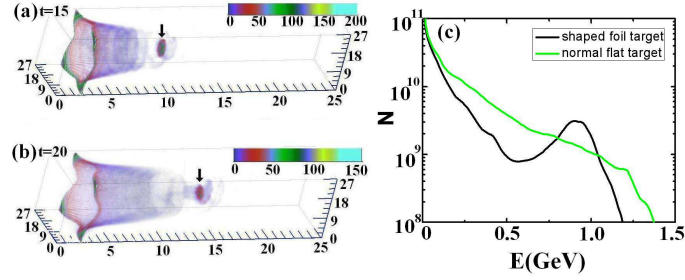


FIG. 4: Proton density distributions in three dimensional simulations at $t = 15T_0$ (a) and $20T_0$ (b). The single-headed arrow indicates the high quality proton bunch with a higher energy and better collimation. The initial target with $\sigma_T = 6\lambda$ is located between $x = 2.0\lambda$ and 2.3λ , irradiated by a CP laser pulse with $\sigma_L = 8\lambda$. (c) Proton energy spectra at $t = 20T_0$. Here, the normal flat target with $l_0 = l_1 = 0.3\lambda$ is located at the same position as the shaped foil target and is irradiated by the same laser pulse.

value, so it is opaque to the laser pulse and the whole target belongs to the deformation region. We will demonstrate these in the following PIC simulations.

By use of Eq. (6) we can also get the final size of the accelerated ion bunch in the target center. For the present target shape the calculated bunch radius is: $r_b = \sigma_L \sigma_T \sqrt{\ln[\pi n_0 l_0 a_0^{-1} \sqrt{(1 + \beta_e)/(1 - \beta_e)}] (\sigma_L^2 - \sigma_T^2)^{-1}}$, where $\beta_e = \alpha \beta_h$ and α is a function of ion mass and laser intensity. Theoretically it can be obtained from Fig. 1(b) in which $\alpha \approx 0.5$. However in the PIC simulations we find the accelerated bunch size can be approximated much better when we choose $\alpha \approx 1$. This difference may result from our too strict criterion for the minimum target thickness. From the calculated bunch size we can also get requirements for the shape factors, such as $\sigma_T < \sigma_L$ and $l_1 \leq l_0 \times \exp(-r_b^2/\sigma_T^2)$. In the next section we present results of multi-dimensional PIC simulations, compare them with the above results and use them to get the optimal shape factors.

A. Particle-in-cell simulations

We use the VLPL code to do both 2D and 3D simulations [27]. First, we do 3D-simulation to show the ion acceleration from the shaped foil target. and then we investigate in detail the effects of the target parameters on the beam quality by less time-consuming 2D simulations.

The simulation box in the 3D-simulation is $25\lambda \times 27\lambda \times 27\lambda$, which consists of $2500 \times 225 \times 225$ cells. A circularly polarized laser pulse with a Gaussian profile in space and a trapezoidal profile (linear growth - plateau - linear decrease) in time is normally incident on the foil target. The temporal profile satisfies:

$$a = \begin{cases} a_0 \exp(-\frac{y^2}{\sigma_L^2})t, & 0 \leq t < 1T \\ a_0 \exp(-\frac{y^2}{\sigma_L^2}), & 1T \leq t \leq 6T, \\ a_0 \exp(-\frac{y^2}{\sigma_L^2})(8-t), & 6T < t \leq 7T, \end{cases} \quad (10)$$

where $a_0 = 100$ is the normalized intensity of the laser electric field, $\sigma_L = 8\lambda$ is the focal spot radius, $T = 3.3fs$ is the laser cycle for an infrared laser with $1\mu m$ wavelength. The initial target is located between $x = 2.0\lambda$ and 2.3λ , with a transversely varying thickness, as shown in Fig. 2. Here, the cutoff thickness $l_1 = 0.15\lambda$ and $\sigma_T = 6.0\lambda$. The plasma density is $n_0 = 100$.

Fig. 4 presents the proton density distributions at two time points: $t = 15T_0$ and $20T_0$. One sees that the center part of the target is accelerated strongly and soon breaks away from the whole target. As expected, the deformation of the target center is well suppressed and a peak appears in the proton energy spectrum, which is shown in Fig. 4(c). The number of the protons whose energy is larger than $0.65GeV$ is about 8.3×10^{11} and their total energy is about $120J$. Instead, for a usual flat target, the energy spectrum shows a typical exponential decay due to the easy heating and deformation of the target. By diagnosing the divergency angle distribution, the average divergency of these energetic protons from the shaped foil target is less than 5° . The whole target can be stably accelerated until the end of laser irradiation with the energy conversion efficiency as high as 23.1% .

In Fig. 4(a,b), it is easy to distinguish the deformation region, acceleration region and transparency region. The center part is the acceleration region, which composes the energy peak in the spectrum. Around it is the transparency region, where the electron density is quickly low enough so that the laser pulse can easily penetrate it and then go through it. This region separates the acceleration region from the deformation region locating in the outer side of the target and effectively suppresses the target heating and protects the acceleration region. For a flat target, this transparency region can also be formed due to the density dilution during the target deformation. However, the process is much slower and it is a gradual changing. Target heating is inevitable then, and there is no obvious acceleration region formation. The pre-shaped target makes the final isolated acceleration bunch possible. The radius of the bunch in our simulation is around 4.5λ , which is close to the theoretical estimate for r_b .

Although our 3D simulations show the possibility of a GeV monoenergetic proton beam acceleration, a well shaped target is required. In experiment, it may be difficult to make a well matched target without any deviations. Certainly, the final beam quality should be related with the target shape factors. For real applications, we are going to demonstrate the robustness of this shaped target scheme. In the following we discuss in detail the effects of these factors on the final beam bunch. To save the computational time, we only perform 2D simulations to show the effects. A series of 2D simulations have been performed. The whole simulation box is $32\lambda \times 32\lambda$, sampled by 3200×3200 cells. The foil target initially locates between $x = 5.0\lambda$ and 5.3λ . The CP laser pulse has the same profile both in time and space as above 3D case except the pulse duration is now $\tau = 10$, which corresponds to a distribution of 1T-8T-1T in time.

B. Dependence on the shape factor

We first take into account the influence of the cutoff thickness l_1 on the beam quality. In the simulation we fix all other parameters and only change l_1 . The ratio of the target width to the laser focus (σ_T/σ_L) is kept to be $7/8$. Fig. 5 shows the simulation results. We can see that the spatial energy distribution in Fig. 5(a) and (b) are almost the same. The cutoff thicknesses for these two cases are 0.05λ and 0.15λ , respectively. The corresponding energy spectra are shown in Fig. 5(d). Again, the energy distributions of high energy protons for these two cases are the same. However, when l_1 is increased to 0.25λ , the energy spectrum changes significantly as shown in Fig. 5(d). The peak energy decreases and the cutoff energy increases. The spectrum tends to be the one of a flat target. It shows there exists a threshold value for l_1 . When l_1 is larger than the threshold, the spectra are significantly different. In additional simulations, we find that the threshold is about 0.20λ in the present case. This is close to the theoretical value of our analysis above. When the cutoff thickness is smaller than the $l_0 \times \exp(-r_b^2/\sigma_T^2)$, the accelerated bunch size is almost constant as shown in Fig. 5(a) and (b). When it increases, no obvious transparency region separates the acceleration and the deformation regions. Target deformation happens continuously along the target and the effectively accelerated bunch is smaller as shown in Fig. 5(c) and the final spectrum is close to the flat target case.

The most important factors are the matching parameters: σ_T and σ_L . In the following we check their effects on the beam quality. Fig. 6 shows some typical simulation results for different σ_T and σ_L . The top four figures show the

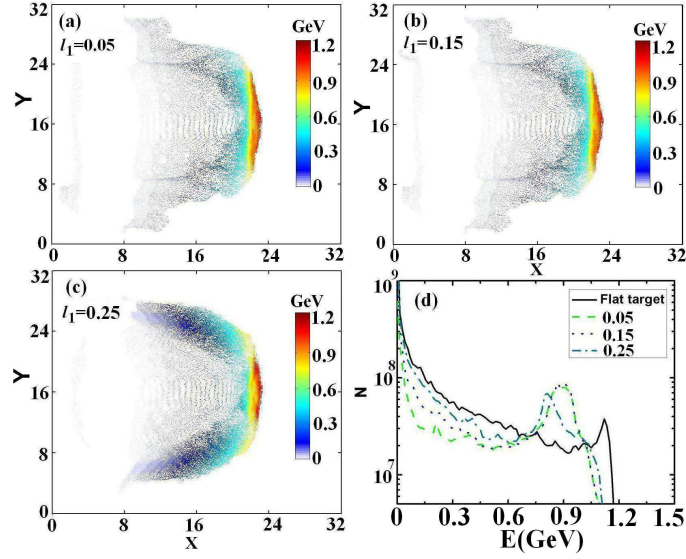


FIG. 5: Proton energy distributions in x-y space for different cutoff thickness l_1 : (a) 0.05λ , (b) 0.15λ and (c) 0.25λ . All the other laser pulse and target parameters are the same. (d) Proton energy spectra at $t = 30T_0$. Here the flat target refers to the one with $n_0 = 100$ and $l_0 = l_1 = 0.3\lambda$.

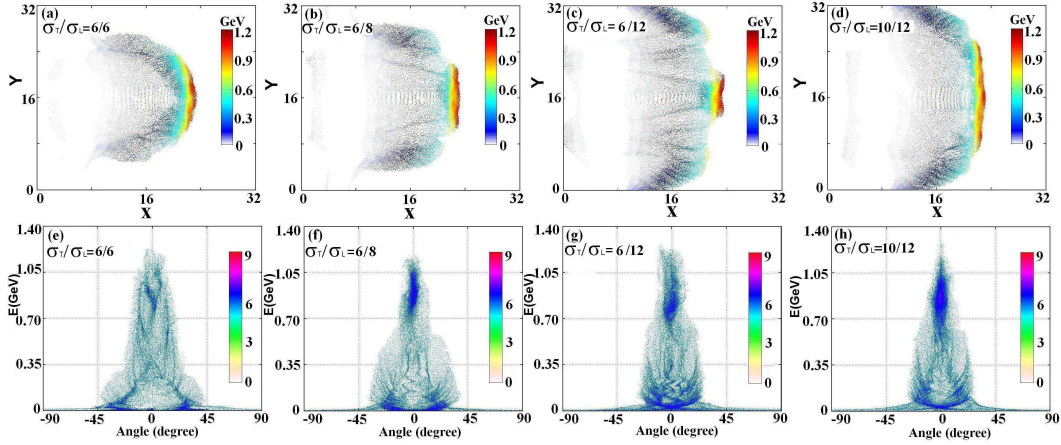


FIG. 6: Proton energy distributions in x-y space for different σ_L and σ_T at $t = 30T_0$: (a) $\sigma_L = 6\lambda$, $\sigma_T = 6\lambda$, (b) $\sigma_L = 8\lambda$, $\sigma_T = 6\lambda$, (c) $\sigma_L = 12\lambda$, $\sigma_T = 6\lambda$, and (d) $\sigma_L = 12\lambda$, $\sigma_T = 10\lambda$. Corresponding proton energy distributions as a function of the divergence angle are shown in (e)-(h).

proton energy distributions in space while the bottom four correspond to the angular distributions. We fix $\sigma_T = 6\lambda$ and increase σ_L from 6λ to 12λ . It is shown that, when σ_T is close to σ_L , the target deformation happens. Most protons are located at the deformation region and the target evolves into a natural cone. The corresponding energy-divergency distribution is widely spread, as shown in Fig. 6(e). With the increase of laser focus, the center part of the target is uniformly accelerated so that it can break away from the whole target. The three regions mentioned before can be easily distinguished from the Fig. 6(b-c). A bunch of protons with a higher energy and a better collimation is formed in Fig. 6(f-g). The radius of the bunch decreases with σ_L , which confirms the theoretical analysis. When σ_L increases, the transparency region extends to the target center, a larger laser focus (or laser energy) leads to a smaller accelerated bunch. The results show the importance of a well matched target. Fig. 6(d) and (h) correspond to a well matched case when the laser focus is $\sigma_L = 12\lambda$. When we increase the target width close to the σ_L , the acceleration region broadens and more ions are uniformly accelerated. Fig. 7 shows both the energy spectra and the angular distributions for these cases. As expected, there is a clear quasi-monoenergetic peak both in the case with $\sigma_T/\sigma_L = 6/8$ and $\sigma_T/\sigma_L = 10/12$. The peak energy is about 0.85GeV and 0.80GeV , respectively. The corresponding full-width of half maximum divergence angle is about 6° and 4° . Obviously, for the well matched cases the larger the laser focus, the more the accelerated protons. On the contrary, for the not perfect matched case, both the peak

TABLE I: Available and optimum values of σ_T/σ_L

σ_L	σ_T/σ_L						
	Available values						Optimum
6	0.5	0.583	0.677	0.75	0.833	0.916	0.75
8	0.375	0.5	0.6	0.75	0.8125	0.875	0.8125
10	0.4	0.5	0.6	0.7	0.8	0.9	0.8

energy and the total production of the accelerated protons decrease. For the unmatched case, no clear peak appears and the proton number decreases further.

In order to obtain the optimal ratio of σ_T/σ_L in the simulation, we perform the parameter scanning as shown in Table I. Here, all the target and laser parameters are the same except for σ_T and σ_L . The available values of σ_T/σ_L mean that a high quality proton bunch with a quasi-monoenergetic peak and low divergency angle can be observed with these parameters. The optimum value indicates the best bunch quality such as the narrowest energy spread and the lowest divergency. It is shown that the tolerable values of σ_T/σ_L exist around 0.50-0.90 while the optimum value is about 0.80. These simulations supplement our analytical results which only give the condition of $\sigma_T/\sigma_L < 1$ and also give some quantitative illumination to the experiments.

C. Effect of target surface roughness

Since in our scheme, the target thickness is less than the laser wavelength, i.e. nanometer-thickness, the relatively larger surface roughness of the target might be inevitable in real experiments and it may have influence on the final accelerated ion beam. Here we check its effects by comparing three simulations with different surface roughness: (a) a smooth surface, (b) 10% roughness and (c) 30% roughness. The initial targets are shown in Fig. 8(a). In order to resolve the surface roughness, both the longitudinal and transversal cell sizes should be small enough which leads to extremely small steps both in space and time in the simulation. This makes the simulations extremely time consuming. Therefore, we only present the simulation results at an early time $t = 10T_0$. This time is, however, already long enough to see the final effects. Fig. 8(c) shows proton energy spectra for these cases. We notice that all the spectra show a clear energy peak despite the different surface roughness. Yet, for the target with 30% surface roughness, the peak energy is about 0.25GeV, which is higher than the value of 0.2GeV in the cases with a lower roughness. Similarly, the cutoff energy is also higher than the other two cases. The differences between the two lower roughness cases are much smaller. The main effect of the target roughness is increasing the laser absorption and conversion efficiency of its energy to the super hot electrons. These electrons are easily dispersed in space and awake the TNSA acceleration. This can be seen in Fig. 8(b), in which the energy spectrum of the electrons is shown. Obviously the target with 30% roughness has a much higher electron temperature. The other two cases are similar. In addition to the spectrum we also check the angular distribution. The results are shown in Fig. 8(d). There is no obvious difference with the case of smooth target and a target with 10% roughness. So generally speaking, the simulation shows the roughness of 10% is acceptable. It gives a quantity guidance for experimental demonstrations.

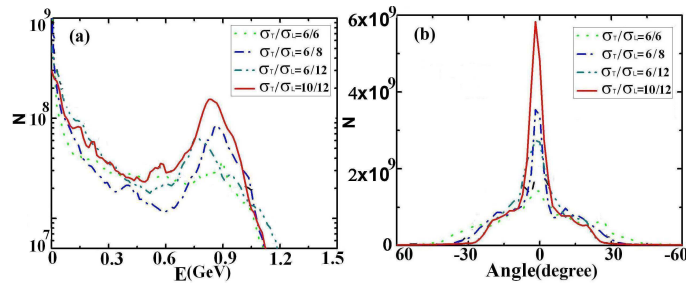


FIG. 7: Proton energy spectra (a) and divergency angle (b) distributions for different laser focus radii σ_L and σ_T at $t = 30T_0$.

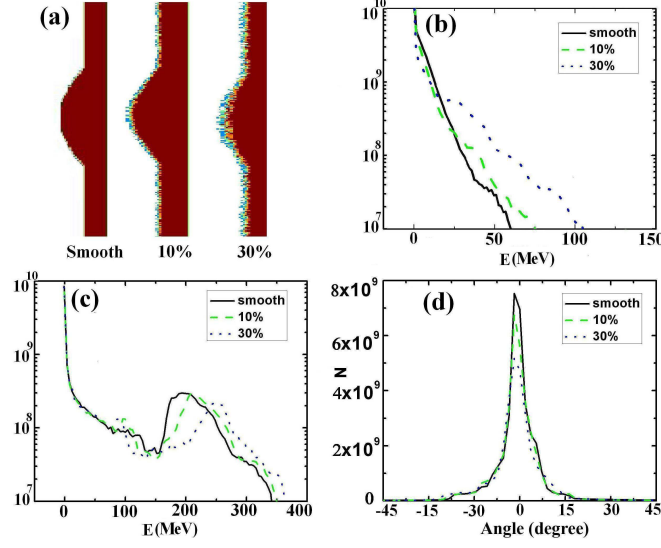


FIG. 8: Shaped foil targets with different surface roughness (a). Electron energy spectra (b) and proton energy spectra (c) for different surface roughness at $t = 20T_0$. Proton divergency angle distributions at $t = 20T_0$ (d). Here, the cutoff thickness for these cases is 0.15λ .

D. Radiation damping effect

Further, we perform simulations to check the radiation damping effects, which was found to be very important for transparent nano targets [28]. To simulate the damping effect we suppose that, at any given moment of time, the electron radiation spectrum is synchrotron like [29]. The critical frequency ω_c is given by the relation $\omega_c = (3/2)\gamma^2|\Delta P_\perp|/(mcdt)$; ΔP_\perp is the variation of transversal electron momentum force during the time step of dt . In our PIC code, we follow trajectories of each electron and calculate the emission during the interaction. We calculate the damping effects by considering the electron's recoil due to the emitted radiation. The recoil force was included in the equations of electron motion. We do 3D simulations with the same parameters as mentioned above, while the radiation module switched on this time.

Fig. 9 shows the synchrotron radiation distribution. θ is the angle between the directions of photon emission and laser propagation; ϕ is the azimuthal angle. We find that the emitted x-ray photons are mainly radiated at the angle of $(\theta = 35^\circ - 45^\circ)$. Totally 8J energy (about 1.54% of the laser energy) is transferred to the x-ray photons with the average photon energy about 1.2MeV. For the electrons' cooling, our simulation shows that there is no obvious changing in the final electron energy spectrum. Only the highest electrons ($400\text{MeV} < E_k < 800\text{MeV}$) are a little cooling down. The total electron energy is about 0.123J less than the one in the simulation without the radiation effect. This means the electrons can quickly get back their radiation-lost energy from the driving pulse. For the ion acceleration, our simulation results show there is almost no observable difference in the final ion spectra between the cases with and without radiation damping effects. Obviously this little electron cooling can not benefit the ion acceleration so much for these laser-plasma parameters.

IV. DISCUSSION AND SUMMARY

We should point out that the target shaping only helps to reduce electron heating and keeps the acceleration much more uniform and for a longer time. However, the instabilities still exist [26, 30] in the accelerated plasmas. Although under perfect matching condition proton numbers can be increased by increasing the laser focus as Fig. 6(d) suggests, the surface instability will develop after some time and destroy the acceleration structure, which limits the final proton energy. Suppression of such kinds of instabilities should be an important work both for the laser ion acceleration itself and for the fast ignition of inertial fusion targets based on laser-accelerated ion beams [7]. These are important issues for the future work.

In summary, by multi dimensional PIC simulations, we have checked the target shape effects on GeV mono-energetic proton beam acceleration. We propose to use a shaped target to match the laser intensity. By this, there will be a transparency region separating the acceleration region and deformation region and keeping the acceleration structure

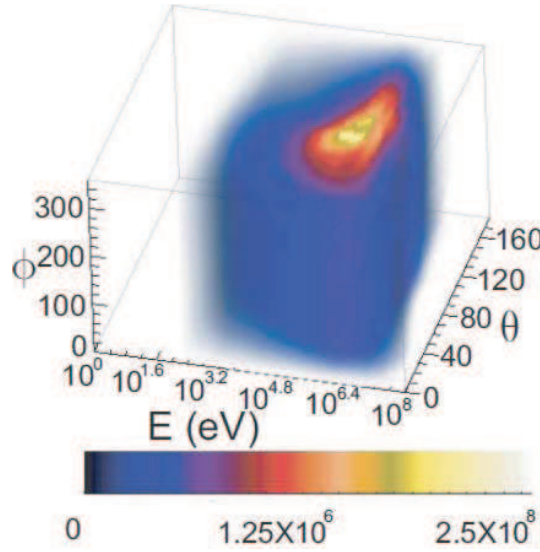


FIG. 9: Synchrotron radiation distribution in the angular-energy space at $t = 20T_0$. The colorbar represents the photon number.

for a longer time compared with a usual flat target. Final spectrum shows a well mono-energetic peak once the well shaped target is used. Effects of shape factors and target surface roughness are also checked, which demonstrates the robustness of our scheme. Finally, synchrotron radiation and damping are checked. It does little influence on the ion acceleration for the present parameter region.

Acknowledgments

This work is supported by the DFG programs TR18 and GRK1203. MC acknowledges support by the Alexander von Humboldt Foundation. TPY thanks the scholarship awarded by China Scholarship Council(CSC NO. 2008611025). ZMS is supported in part by the National Nature Science Foundation of China (Grants No. 10674175, 60621063) and the National Basic Research Program of China (Grant No. 2007CB815100).

-
- [1] A. Pukhov, Phys. Rev. Lett. **86**, 3562 (2001); B.M. Hegelich, *et al.*, Phys. Rev. Lett. **89**, 085002 (2002); J. Fuchs, *et al.*, Nature Phys. **2**, 48 (2006); B.M. Hegelich, *et al.*, Nature (London) **439**, 441 (2006); Y. Lin, *et al.*, Phys. Plasmas, **14**, 056706 (2007).
 - [2] J. Denavit, Phys. Rev. Lett. **69**, 3052 (1992); L. O. Silva, *et al.*, Phys. Rev. Lett. **92**, 015002 (2004); M. Chen, *et al.*, Phys. Plasmas **14**, 053102 (2007); M. Chen, *et al.*, Phys. Plasmas **14**, 113106 (2007); M.Q. He, Q.L. Dong, Z.M. Sheng, *et al.*, Phys. Rev. E **76**, 035402(R) (2007).
 - [3] T. Esirkepov, *et al.*, Phys. Rev. Lett. **92**, 175003 (2004).
 - [4] T. Ditmire, *et al.*, Nature **386**, 54 (1997); M. Zepf, E.L. Clark, F.N. Berg, *et al.*, Phys. Rev. Lett. **90**, 064801 (2003); J. Zheng, K. Mima, Z.M. Sheng, *et al.*, Phys. Plasmas **15**, 053106 (2008); L. Cao, *et al.*, Phys. Rev. E **78**, 036405 (2008).
 - [5] E. Fourkal, *et al.*, Med. Phys. **34**, 577 (2007).
 - [6] M. Borghesi, *et al.*, Phys. Plasmas **9**, 2214 (2002).
 - [7] N. Naumova, *et al.*, Phys. Rev. Lett. **102**, 025002 (2009); M. Roth *et al.*, Phys. Rev. Lett. **86**, 436 (2001); T.
 - [8] T. Toncian *et al.*, Science **312**, 410 (2006).
 - [9] S. Gordienko, T. Baeva, A. Pukhov, Phys. Plasmas **13**, 063103 (2006).
 - [10] T. Esirkepov, *et al.*, Phys. Rev. Lett. **89**, 175003 (2002).
 - [11] H. Schwöerer, *et al.*, Nature **439**, 445 (2006).
 - [12] S.V. Bulanov, *et al.*, Plasma Phys. Rep. **28**, 453 (2002).
 - [13] T. Okada *et al.*, Phys. Rev. E **74**, 026401 (2006).
 - [14] A.P.L Robinson, *et al.*, Phys. Rev. E. **75**, 015401(R), (2007); R. Sonobe *et al.*, Phys. Plasma. **12**, 073104 (2005); T.P. Yu *et al.*, Phys. Plasma. **16**, 033112 (2009).
 - [15] A. Macchi, *et al.*, Phys. Rev. Lett. **94**, 165003 (2005).
 - [16] X. Zhang, *et al.*, Phys. Plasmas **14**, 073101 (2007).

- [17] O. Klimo, *et al.*, Phys. Rev. Special Topics - Accelerators and Beams **11**, 031301 (2008).
- [18] A. P. L. Robinson, *et al.*, New J. Phys. **10**, 013021 (2008).
- [19] X.Q. Yan, *et al.*, Phys. Rev. Lett. **100**, 135003 (2008).
- [20] X. Zhang, *et al.*, Phys. Plasmas **14**, 123108 (2007).
- [21] B. Qiao, *et al.*, Phys. Rev. Lett. **102**, 145002 (2009).
- [22] V.K. Tripathi, *et al.*, Plasmas Phys. Control. Fusion **51**, 024014 (2009)
- [23] M. Chen, A. Pukhov, T.P. Yu, and Z.M. Sheng, to be published in Phys. Rev. Lett.(2009).
- [24] A.P.L Robinson, *et al.*, Plasma Phys. Control. Fusion **51**, 024004, (2009).
- [25] A.A. Gonoskov, *et al.*, Phys. Rev. Lett. **102**, 184801 (2009).
- [26] F. Pegoraro, *et al.*, Phys. Rev. Lett. **99**, 065002 (2007).
- [27] A. Pukhov, J. Plasma Phys. **61**, 425 (1999).
- [28] V.V. Kulagin, *et al.*, Phys. Rev. Lett. **99**, 124801 (2007).
- [29] S. Kiselev *et al.*, Phys. Rev. Lett. **93**, 135004 (2004).
- [30] M. Chen, *et al.*, Phys. Plasmas **15**, 113103 (2008).